MATERIALS SCIENCE

Surface premelting and melting of colloidal glasses

Qi Zhang[1], Wei Li[1], Kaiyao Qiao[1], Yilong Han[1,2]*

The nature of liquid-to-glass transition is a major puzzle in science. A similar challenge exists in glass-to-liquid transition, i.e., glass melting, especially for the poorly investigated surface effects. Here, we assemble colloidal glasses by vapor deposition and melt them by tuning particle attractions. The structural and dynamic parameters saturate at different depths, which define a surface liquid layer and an intermediate glassy layer. The power-law growth of both layers and melting front behaviors at different heating rates are similar to crystal premelting and melting, suggesting that premelting and melting can be generalized to amorphous solids. The measured single-particle kinetics reveal various features and confirm theoretical predictions for glass surface layer.

INTRODUCTION

Glass melting is not a reverse process of liquid-to-glass transition, i.e., vitrification or glass transition. For example, strains can exist in the solid parent phase during melting but not in the liquid parent phase during vitrification (*1*); the heat capacity of glass exhibits hysteresis upon cooling and heating (*2*, *3*); rapidly quenching liquid produces glass, whereas heating glass at the same rate may produce crystal, i.e., devitrification, rather than melting (*4*). In contrast to the intensively studied glass transition, the study about glass melting is at the preliminary stage (*5*–*11*). For ordinary glasses, liquids usually homogenously form within bulk via a nucleation-like process and grow with Avrami-type kinetics (*7*, *9*), whereas melting at free surfaces (i.e., vapor-solid interfaces) is negligible compared with melting in large bulk (*5*). By contrast, ultrastable glasses exhibit heterogeneous surface melting (*5*, *8*, *10*, *12*–*14*). A crystal surface usually forms a thin liquid layer slightly below the melting temperature T_m, i.e., surface premelting (*15*). Such surface liquid propagates into bulk when $T \geq T_m$, i.e., surface melting, and preempts melting from within. Surface melting has been studied in atomic and molecular ultrastable glasses (*5*, *8*, *10*, *16*) but lacks microscopic measurement, comparison with crystals, and a quantitative theory. In glass melting, the glass transition temperature T_g plays the role of T_m in crystal melting (*2*, *5*, *8*, *17*), but whether glass exhibits surface premelting has not been explored.

Besides melting, glass surface behaviors, such as the surface mobile layer, are key topics in studies on molecular (*5*), metallic (*18*), and polymer (*19*) thin-film glasses. The surface mobile layer has been studied by comparing the behaviors of thin-film glasses with different thicknesses or other methods without single-particle resolution (*20*). Consequently, how different it is from a normal liquid and how local properties vary with depth remain unclear (*21*, *22*).

Colloids are outstanding model systems, because micrometer-sized particles and their thermal motions can be visualized and tracked by optical microscopy (*23*). Colloids have provided important microscopic information on bulk glasses (*24*), such as shear-induced bulk glass melting (*6*). The studies about glass surfaces are mainly near a fixed wall (*25*, *26*), and the free surface of glass has only been experimentally explored using repulsive colloidal particles during vapor deposition under gravity at a fixed temperature (*27*). Thermally induced bulk or surface melting has not been explored at the single-particle level, as it requires colloids with tunable attractions. Colloids with tunable attractions have been achieved by thermal-sensitive depletant (*28*), Casimir effect (*29*), DNA (*30*), and electric field (*31*). Here, we use attractive colloids whose dye-induced long-range attraction is tunable in 0 to 1 Boltzmann constant (k_BT) (*23*) and measure the microscopic kinetics at different effective temperatures. Premelting and melting driven by weakening particles' attractions are compared under slow and fast temperature changes for monolayer and multilayer samples.

RESULTS

We use 50:50 mixture of poly(methyl methacrylate) (PMMA) spheres with diameters of σ_a = 2.08 μm and σ_b = 2.74 μm to avoid crystallization. A dye is added to induce the depletion-like attraction between PMMA spheres (Fig. 1) (*23*). As temperature decreases, the dye is pumped to the unheated region due to thermophoresis, thus the attraction strength $|U_{min}|$ decreases (*23*), and the effective temperature $T_{eff} = k_BT/|U_{min}|$ increases linearly (Fig. 1B). Monolayer and multilayer colloids are confined between two centimeter-sized parallel glass plates with different separations in the *z* direction. Here, monolayer and multilayer refer to the layers in the *z* direction, whereas liquid or glassy layer refers to the layer in the *y* direction defined in Fig. 2A (fig. S3). The colloidal glasses are assembled via vapor deposition at a typical growth rate of 0.5 σ/t_0, which well lies in the range of <100 for the formation of ultrastable molecular glasses (section S1 and movie S1) (*32*). t_0 is the mean time for a particle on the vapor-liquid interface moving one mean diameter $\sigma = (\sigma_a + \sigma_b)/2$. Approximately 10^4 particles are observed in the field of view by optical microscopy, and their Brownian motions are tracked by image analysis (*33*). The measurements below are made after the vapor deposition process. All the three monolayer samples show similar results. Experimental details are provided in Materials and Methods.

Structural and dynamic parameters

Each particle *i* at depth *y* is characterized by two structural parameters [local density ρ_i (Fig. 2, A and C) and two-body local excess

[1]Department of Physics, Hong Kong University of Science and Technology, Hong Kong, China. [2]Hong Kong University of Science and Technology, Shenzhen Research Institute, Shenzhen 518057, China.
*Corresponding author. Email: yilong@ust.hk

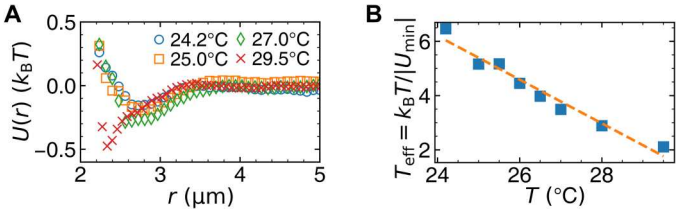

Fig. 1. Pair potentials of PMMA spheres. (**A**) Pair potential $U(r)$ as function of center-to-center distance at 27°C extracted from radial distribution function $g(r)$ (fig. S1). (**B**) The effective temperature of 2.08-μm-diameter poly(methyl methacrylate) (PMMA) spheres $T_{eff} = k_BT/|U_{min}|$ decreases with the sample temperature T. U_{min} is the minimum of the measured $U(r)$. Dashed line, linear fit; k_BT, Boltzmann constant.

entropy s_{2i} (*34*)] and three dynamic parameters [structural relaxation time $\tau(y)$, Debye-Waller factor DW_i (Fig. 2, B and D) (*27*), and hop indicator function p_{hi} (*35*)] (Fig. 2E). $\rho_i \equiv \pi\sigma_i^2/(4A_i)$ where A_i is the area of particle i's Voronoi polygon. s_{2i} reflects the number of inherent structures (*36*). The entropy of a system can be viewed as the sum of the ideal gas entropy and the excess entropy s_{excess}. $s_{excess} = s_2 + s_3 + s_4 + \cdots$ where s_n is the n-body contribution to entropy (*37*). s_2 contributes 80 to 90% of s_{excess} (*38*). Structural relaxation time τ, i.e., the decay time of self-intermediate scattering function F_q, is measured from the fitting $F_q(t, y) \sim e^{-(t/\tau)^\beta}$ (fig. S9). It is proportional to viscosity, which is a dynamic quantity. A particle's vibration amplitude is described by

$$DW_i(t) = \sqrt{\langle[\vec{r}_i(t) - \langle\vec{r}_i(t)\rangle]^2\rangle}/\sigma \quad (1)$$

where $\langle\vec{r}_i(t)\rangle$ is the average position during $[t - t_0/2, t + t_0/2]$. t_0 is chosen as 30 s, because the out-of-cage time near the surface is about 30 s (fig. S10). Using other time intervals such as 100 or 200 s does not change the results (fig. S11). We also calculate the cage-relative Debye-Waller factor DW_{cr} in Eq. 11 based on the local coordinate of each particle's neighboring partcicles (*39*). DW and DW_{cr} give similar results (fig. S23), indicating that the long-wavelength fluctuations (*40*, *41*) are not important to our results. Particle's jumping ability can be described by the hop indicator function $p_{hi}(t) = \sqrt{\langle[\vec{r}_i(t) - \langle\vec{r}_i(t)\rangle_{t_B}]^2\rangle_{t_A}\langle[\vec{r}_i - \langle\vec{r}_i\rangle_{t_A}]^2\rangle_{t_B}}/\sigma$ (*42*), where t_A and t_B represent the time intervals $[t - t_0/2, t]$ and $[t, t + t_0/2]$, respectively. DW and p_h reflect the short-time dynamics, while τ reflects the long time scale for structural relaxation.

We measure $\log(\tau)$, $\log(DW)$, and $\log(p_h)$, because they are commonly used in glass studies (*35*, *43*). Using $\{\rho, s_2\}$ or $\{\log(\rho), \log(|s_2|)\}$ yields similar results (fig. S15 and movie S4). All the five parameters are normalized (denoted by ~) from 0 (vapor) to 1 (bulk glass) for comparison (Materials and Methods).

Slow temperature change

T_g is quasistatically approached by decreasing temperature at $\Delta T = 0.2$°C per step with 1 to 3 hours of equilibration at each step. Thus, the observed phenomena are equilibrium features near the surface. N quantities may saturate to their bulk values at different depths, which define N layers near the surface. All the structural parameters $\{\tilde{\rho}, \tilde{s}_2\}$ saturate to their bulk values at y_1, and all the long-time $[\log(\tilde{\tau})]$ and short-time $\{\log(\tilde{DW}), \log(\tilde{p}_h)\}$ dynamic parameters saturate at y_2 (Fig. 2E). Their profiles define a dense vapor layer at $5\% < \tilde{\rho} < 50\%$ with thickness $y_0 - y_s$, a surface liquid layer at $50\% < \tilde{\rho} < 95\%$ with thickness $d_1 = y_1 - y_0$, and an intermediate glassy layer at $\tilde{\rho} \geq 95\%$ and $\log(\tilde{DW}) < 95\%$ with thickness $d_2 - d_1 = y_2 - y_1$ (see $y_{s,0,1,2}$ defined in Fig. 2E). Similar double surface layers with an unexpectedly large thicknesses of more than 100 particles have recently been observed in glasses (*27*, *44*).

$d_{1,2}$ represents the penetration depths of the surface effect on structure and dynamics, respectively. Figure 3A shows

$$d_{1,2} \propto (T/T_{g1,2} - 1)^{\alpha_{1,2}} \quad (2)$$

The fitted $T_{g1} = T_{g2} = 25.3$°C is consistent with the directly observed complete bulk melting at 25.3°C (movie S2). Moreover, the bulk density jumps and elastic moduli approach zero at 25.3°C (fig. S14), similar to operationally defined glass transition temperature at the sudden change in thermal expansion, shear modulus, or other properties under heating or cooling (*2*). Note that T_g is derived from $d_{1,2}$ via Eq. 2, which circumvents the ambiguity of distinguishing

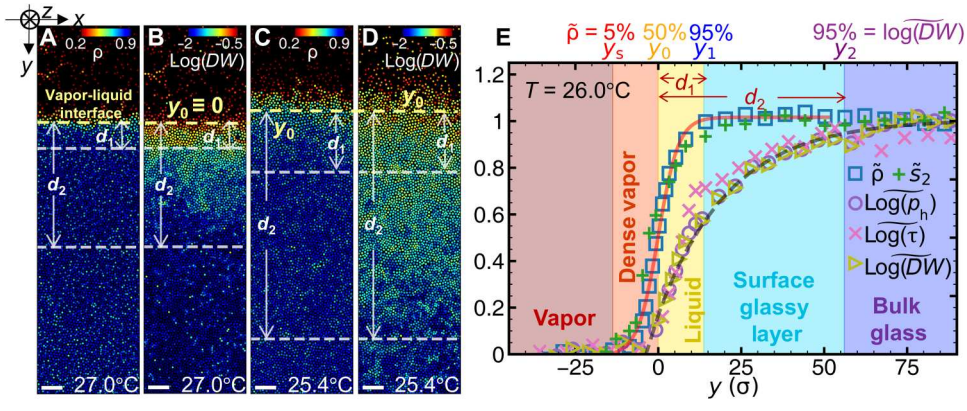

Fig. 2. Surface premelting under slow temperature change. At 27.0° (**A** and **B**) and 25.4°C (**C** and **D**), particles in the monolayer are colored by ρ and log(*DW*), respectively. Scale bars, 20 μm. (**E**) At 26.0°C, the profiles of the structural parameters $\{\tilde{\rho}(y)$ and $\tilde{s}_2(y)\}$ fitted by Eq. 3 (red solid curve); the profiles of the dynamic parameters $\{\log[\tilde{\tau}(y)]$, $\log[\tilde{p_h}(y)]$, and $\log[\tilde{DW}(y)]\}$ fitted by Eq. 4 (black dashed curve). The five regimes (vapor, dense vapor, liquid, glassy layer, and bulk glass) have four interfaces labeled on the top *x* axis; their positions $y_{s,0,1,2}$ are defined at $\tilde{\rho} = 5$, 50, and 95% and $\log(\tilde{DW}) = 95\%$, respectively. $y = 0$ is defined as y_0 at 27.0°C [yellow dashed lines in (A) and (B)].

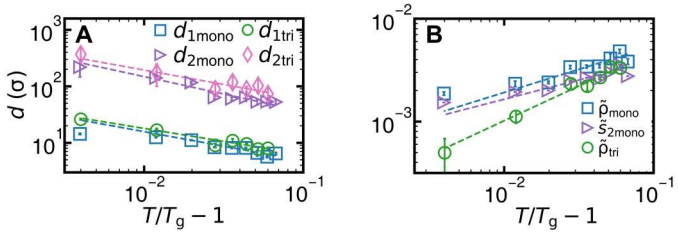

Fig. 3. Power laws of surface premelting under slow temperature change. (**A**) Layer thicknesses $d_{1,2}$ fitted by Eq. 2 (dashed lines) with T_g = 25.3°C, α_1 = 0.51 ± 0.09, α_2 = 0.61 ± 0.10 for the monolayer and T_g = 25.0°C, α_1 = 0.46 ± 0.10, α_2 = 0.51 ± 0.12 for the trilayer. (**B**) $\tilde{\rho}_{y=y_s'}(T)$ and $\tilde{s}_{2,y=y_s'}(T)$ fitted by Eq. 7 with β_ρ = 0.45 ± 0.10 and β_{s_2} = 0.38 ± 0.08 for the monolayer and β_ρ = 0.68 ± 0.09 for the trilayer. The subscript "$y = y_s'$" represents the parameter at the vapor interface y_s' defined by Landau theory (section S3). The subscripts "mono" and "tri" in legends represent the monolayer glass and the trilayer glass, respectively. Note that decreasing T increases the effective temperature.

supercooled liquid and glass. The effective temperature linearly decreases with the sample temperature (Fig. 1B), i.e., $(T_g^{eff} - T^{eff}) \propto (T - T_g)$; thus, $(T - T_g)^\alpha$ in Eq. 2 can be expressed as $(T_g^{eff} - T^{eff})^\alpha$, which maintains the power-law relationship. Different choices of the threshold values (e.g., 95 or 99.5%) only shift $d_{1,2}$ by a constant factor and do not affect the fitted values of T_g and α (fig. S22).

In crystal premelting, the power-law growth of the surface liquid thickness has been predicted in theory (*15*, *45*) and observed in experiments (*15*, *23*) and simulations (*15*, *46*). Here, we find that it also holds for the two layers of the colloidal glass before reaching T_g (Fig. 3A). Premelting has only been discussed for crystals at $\gamma_{vc} > \gamma_{vl} + \gamma_{lc}$. γ is the interfacial energy. The subscripts "vc," "vl," and "lc" represent the vapor-crystal, vapor-liquid, and liquid-crystal interfaces, respectively. Although double layers have not been reported in premelting, they are theoretically possible when $\gamma_{vg} > \gamma_{vl} + \gamma_{lg} > \gamma_{vl} + \gamma_{ls} + \gamma_{sg}$, i.e., forming a liquid (l) layer and a surface glassy (s) layer between vapor (v) and bulk glass (g).

In addition, the profiles of structural parameters, $\tilde{\rho}(y)$ and $\tilde{s}_2(y)$, at different T collapse onto a master curve by rescaling y with $d_1(T)$ (Fig. 4, A and B) and can be fitted by a hyperbolic tangent function

$$\tilde{\rho}(y), \tilde{s}_2(y) = \{1 + \tanh[3(y - y_0)/2d_1]\}/2 \quad (3)$$

The hyperbolic tangent profile commonly exists on vapor-liquid interfaces (*47*), liquid-solid interfaces (*48*, *49*), vapor-solid interfaces (*50*), and solid-solid interfaces (*51*). In addition, error function (erf), the prediction of Landau theory for crystal premelting (*45*), and the Fisk-Widom (FW) function for the interface between fluid phases can fit $\tilde{\rho}(y)$ and $\tilde{s}_2(y)$ equally well (Fig. 4C), because they are in the range of [0, 1] with similar centrosymmetric shapes. The profiles of the dynamic parameters {$\log[\tilde{DW}(y)]$, $\log[\tilde{\tau}(y)]$, and $\log[\tilde{p_h}(y)]$} collapse onto a master curve after y is rescaled by d_2 (Fig. 4, D and E). They are not centrosymmetric and cannot be fitted by Eq. 3. Instead, they can be fitted by both Eqs. 3 and 4

$$f(y) = 1 - \exp[-3(y - y_0)/d_2] \quad (4)$$

$$f(y/d_2) = f(y') = f(y'/\sqrt{2}) = \mathrm{erf}(y') + 2y'\exp(-y'^2)/\sqrt{\pi} - 2y'^2[1 - \mathrm{erf}(y')] \quad (5)$$

where f can represent $\log(\tilde{\tau})$, $\log(\tilde{DW})$, and $\log(\tilde{p}_h)$. Equation 4 has also been observed in the surface relaxation of polymer glasses (*52*, *53*) and a dynamic facilitated lattice model of glass (*54*). It implies that the energy barrier height increases with the depth y exponentially (*53*). Equation 5 is a prediction about log(τ) in the cooperative string model for the glass surface mobile layer (*55*). We find that Eq. 5 has a very similar shape to Eq. 4 and can also well fit the profiles in Fig. 4F.

Relationship between local structure and dynamics

Supercooled liquids generally follow the mode-coupling relation $\tau(T) \propto [\rho_c - \rho(T)]^{-\gamma}$ (*56*). We observe a similar relation

$$\tau(y) \propto [\rho_c - \rho(y)]^{-\gamma} \quad (6)$$

holds near the glass surface at different depths in contrast to different temperatures in the traditional mode-coupling relation (Fig. 5A). The fitted ρ_c = 0.80 is robust to different T and agrees with the mode-coupling transition point of two-dimensional (2D) binary glasses measured in simulations (*57*, *58*) and experiments (*26*, *59*). The fitted ρ_c = 0.80 is smaller than the nonmelted bulk density (≥0.81), which further confirms the premelting. Equation 6 should hold between any dynamic and structural parameters {e.g., $DW(y) \propto [s_{2c} - s_2(y)]^{-\gamma}$} because their profiles collapse (Fig. 4). Furthermore, the low-density region near the surface exhibits the mode-coupling transition behavior of fragile glass, while the high-density region near the bulk exhibits the Arrhenius behavior of strong glass (Fig. 5B). The similar fragile-to-strong crossover as temperature decreases is observed in water (*60*), metallic glasses (*61*), and organic and inorganic glasses (*62*). Structural dynamic correlation is a research focus in the studies of bulk glass and supercooled liquid (*63*); Fig. 5 provides such a connection near the surface.

Figure 3B shows that the structural parameters at the vapor interface vary with temperature in a power law as predicted by Landau theory of crystal premelting (*45*)

$$\tilde{\rho}_{y=y_s'}(T), \tilde{s}_{2,y=y_s'}(T) \propto (T/T_g - 1)^{\beta_{\rho,s2}} \quad (7)$$

Similar to Eq. 2, the power law of Eq. 7 holds after replacing T with T^{eff}. In Landau theory, such power law generally holds for an order parameter near the surface. It has been observed for the sixfold bond-orientational order parameter ψ_6 (*23*) and magnetism (*64*) in crystal premelting but not for ρ and s_2 in crystal or any order parameters in glass before. Figure 3B and fig. S20B show that ρ and s_2 satisfy this power law in monolayer and multilayer glasses. The vapor interface y_s' defined by minimizing the free energy in Landau theory for crystal premelting (*45*) is close to y_s defined by $\tilde{\rho} = 5\%$ (fig. S22).

Multilayer

Monolayer and bilayer colloidal crystals exhibit distinct surface premelting and melting behaviors (*23*), probably because 2D is the critical dimension in which systems have strong long-wavelength fluctuations according to the Mermin-Wagner theorem. However, we find that monolayer and multilayer colloidal glasses have similar behaviors in premelting and melting. This is in accordance with the fact that the results based on DW and DW_{cr} are similar for monolayer samples. The images of multilayer samples are blurry (fig. S17), so we only measure $\tilde{\rho}$ and $\log(DW)$ from the coarse-grained

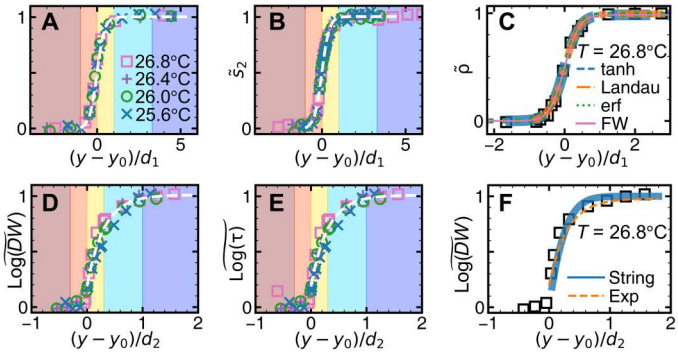

Fig. 4. Profiles perpendicular to the surface of monolayer glass under slow temperature change. $\tilde{\rho}$ profiles (**A**) and $\tilde{s}_2$ profiles (**B**) at different temperatures collapse onto Eq. 3 (white dashed curves). (**C**) The profile of $\tilde{\rho}$ at 26.8°C fitted by hyperbolic tangent function (Eq. 3), the prediction of Landau theory of crystal premelting (eq. S7), error function (erf; eq. S10), and Fisk-Widom (FW) function (eq. S11). Log($\tilde{DW}$) profiles (**D**) and log($\tilde{\tau}$) profiles (**E**) at different temperatures collapse onto Eq. 4 (white dashed curves). (**F**) Log($\tilde{DW}$)profile at 26.8°C fitted by exponential function (Eq. 4) and the prediction of cooperative string model (Eq. 5). The colored regions are labeled in Fig. 2E.

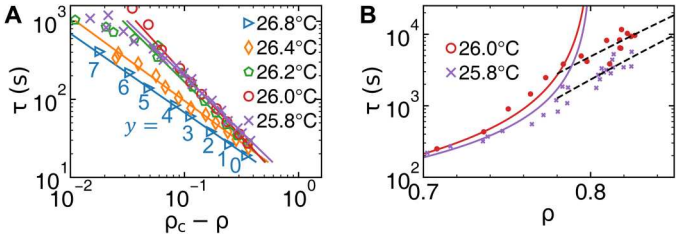

Fig. 5. $\tau(y)$ versus $\rho_c-\rho(y)$ fitted with Eq. 6. (**A**) The fitted $\rho_c = 0.80$ is robust to different temperatures. The depth y is labeled at each data point at $T = 26.8$°C; the data points at other T have similar depths. (**B**) $\tau(\rho)$ follow the mode-coupling transition behavior Eq. 6 (solid curve) at low densities and the Arrhenius behavior $\log[\tau(y)] \propto \rho(y)$ (dashed line) at high densities.

pixel brightness and its fluctuation, respectively (section S2.7). Similar to monolayer samples, Eq. 2 for $d_{1,2}$ and Eq. 7 for surface density hold for the bilayer (fig. S20) and trilayer (Fig. 3, A and B) samples. Their structural and dynamic profiles fit Eqs. 3 and 4, respectively (fig. S19).

Fast temperature change

Crystal melting is usually studied by abruptly increasing the temperature above T_m. Similarly, we abruptly change the temperature controller from 26.5° to 23.3°C across T_g, so that both premelting and melting processes can be studied. $T(t)$ decreases at a rate of about 10^{-3}°C/s (fig. S4).

Similar to the slow temperature change, $d_{1,2}(T)$ under the fast temperature change fits Eq. 2 with $T'_{g1} = T'_{g2} = 23.4$°C (Fig. 6A); $\tilde{\rho}_{y=y'_s}(T)$ and $\tilde{s}_{2,y=y'_s}(T)$ fit Eq. 7 (Fig. 6B). T'_g under the fast temperature change is lower (i.e., attraction weaker and effective temperature higher) than $T_g = 25.3$°C under the slow temperature change, in accordance with the high T_g under rapid quenching in vitrification (*3*). The profiles of the structural and dynamic parameters at different times collapse onto two master curves of Eqs. 3 (Fig. 6C) as well as 4 and 5 (Fig. 6D), respectively. Bilayer and trilayer glasses under the fast temperature change also exhibit similar premelting behaviors (Fig. 6 and figs. S19 and S20).

During the melting stage (Fig. 7), $\rho(y)$ and $\log[DW(y)]$ at each instance still follow Eqs. 3 (Fig. 7, D to G) as well as 4 and 5 (Fig. 7, D to F, and fig. S16), respectively. At $t \geq 3600$ s, the thickness of the glassy layer reaches a constant value (Fig. 7H). The glassy layer can be viewed as the melting front with a hyperbolic tangent density profile (Fig. 7G) and propagates at a constant speed at $t \geq 3600$ s (Fig. 7H). These behaviors agree with the predictions in Landau theory (*65*) and observations in crystal melting experiment (*49*). The constant speed of melting front has also been observed in ultrastable glass melting (*8*, *16*), whereas the constant width of the melting front has only been conjectured in ultrastable glass without an experimental test (*10*). Overlap function has been used to define the glass melting interface in simulation (*8*). We find that it coincides with the interface defined by $\tilde{\rho} = 95\%$ (fig. S12).

Cooperative rearrangement regions

Cooperative rearrangement regions (CRRs) are crucial to glass relaxation (*66*), but the observation of individual CRRs requires single-particle kinetics. We measure CRRs near the surface (Fig. 8 and movie S3). CRRs are defined as clusters composed of at least two mobile particles, i.e., top 10% highest DW particles (*26*, *67*). Particles near the vapor interface move rapidly and much less cooperatively; thus, CRRs are not defined, or the whole region would be one huge CRR. CRRs are rare in the bulk. We measure CRRs in $(y_1 + y_0)/2 < y < y_2$ (Fig. 8).

By assuming that a CRR contains a compact core surrounded by a ramified string-like shell (*66*), the morphology of CRR, i.e., string-like or compact (Fig. 9A), can be described by the fraction of core-like particles p_{core} (Materials and Methods) (*26*). The fraction of core-like particles p_{core} reaches the maximum at 1800 s (Fig. 9B), indicating that the CRR morphology changes from string-like to compact near 1800 s and to string-like thereafter. This morphological change from compact to string-like as effective temperature increases has been predicted (*66*) and observed (*26*) in bulk glasses. Similarly, the glassy layer thickness $(d_2 - d_1)(t)$ shows nonmonotonic behavior and peaks at 1800 s (Fig. 9C). This finding is similar to the observed nonmonotonic dynamic correlation length scale of glasses near a pinned wall (*25*, *26*) or free surface (*68*) accompanied with a similar morphological change of CRRs.

In addition, the major principle axis of the moment of inertia of CRRs changes from parallel to nearly perpendicular to the glass surface at $t > 1800$ s (Fig. 9D), indicating the direction change of CRRs. Such polarized CRRs normal to the surface reflect the transportation of free volumes from surface to bulk, which facilitates the melting (movie S3). In the reverse glass growth via vapor deposition, CRRs were observed to have lower area fractions, i.e., more free volumes, and move from bulk to surface (*27*). These CRRs are similarly elongated normal to the free surface (*27*).

The size distribution of CRRs can be fitted by a power law with exponent γ (Fig. 9E). As the effective temperature increases, γ increases from 0.6 to 1.8, suggesting an increasing fraction of small CRRs. γ reaches a plateau at $t > 2000$ s (Fig. 9F). The measured γ is in the range of [0.5, 2.5] for the power-law exponents of the probability distributions of earthquake magnitudes, i.e., the Gutenberg-Richter law (*69*).

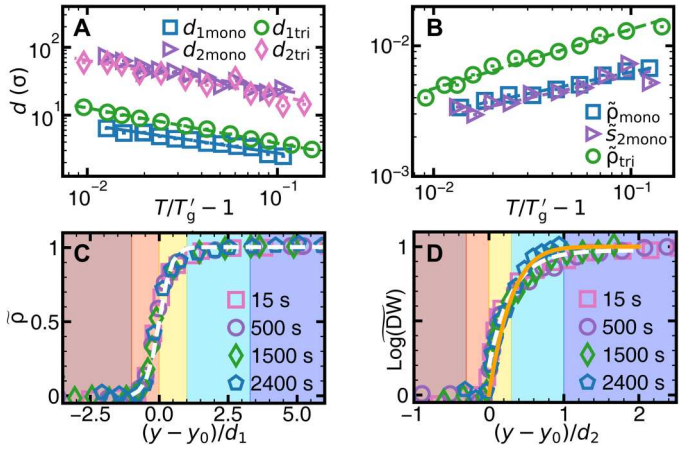

Fig. 6. Surface premelting under fast temperature change. (**A**) Layer thicknesses $d_{1,2}(T) \propto (T/T'_g - 1)^{-\alpha_{1,2}}$ (dashed lines) with the fitted $T'_g = 23.4°C$, $\alpha_1 = 0.42, \alpha_2 = 0.45$ for the monolayer and $T'_g = 24.5°C, \alpha_1 = 0.52, \alpha_2 = 0.52$ for the trilayer. (**B**) $\tilde{\rho}_{y=y'_s}(T)$ and $\tilde{s}_{2,y=y'_s}(T) \propto (T/T'_g - 1)^{\beta_{\rho,s_2}}$ (dashed lines) with the fitted $\beta_\rho = 0.32$ and $\beta_{s_2} = 0.33$ for the monolayer and $\beta_\rho = 0.45$ for the trilayer. The errors are smaller than the symbols. (**C**) $\tilde{\rho}$ at different times collapse onto Eq. 3 (white dashed curve). (**D**) $\mathrm{Log}(\widetilde{DW})$at different times collapse onto Eqs. 4 (white dashed curve) and 5 (orange solid curve). $y_{0,t=0} \equiv 0$. The colored regions are labeled in Fig. 2E.

DISCUSSION

The in situ observations with single-particle kinetics reveal two surface layers. The liquid layer on the surface is stable at a fixed temperature rather than propagating into the bulk, i.e., premelting rather than melting. Note that such identification of premelting does not need the measurement of T_g or any similarity to crystal premelting. Moreover, glass premelting and melting are similar to those of crystals as shown in Table 1, suggesting that premelting and melting theories for crystals could be generalized to glasses. Ordinary glasses exhibit nucleation-like bulk melting similar to crystal melting, which has been suggested as a support of the thermodynamic origin of glass transition (*7*, *9*, *11*). Similarly, because crystal surface premelting is a thermodynamic phenomenon, the similarities between glass and crystal premelting suggest a thermodynamic origin of glass surface premetling. The study of glass surface melting is at the preliminary stage, which lacks theory and experiment at the single-particle level. Simulations mainly focus on the melting front speed and the crossover depth from surface to bulk melting (*8*, *12*–*14*), while glass surface premelting has not been discussed.

Melting is always easier from a free surface than within bulk (section S5). Ultrastable glasses usually melt from surface, which preempts bulk melting, while ordinary glasses usually melt from both surface and bulk. Because bulk region is much larger than surfaces, melting of ordinary glasses is dominated by the bulk. Nevertheless, ordinary glasses have no qualitative distinctions with ultrastable glasses (*70*, *71*) and thus should exhibit similar premelting behaviors, although their surface melting can be easily interrupted by bulk melting. Therefore, a glass with relatively high stability is required for the study of surface melting.

Besides melting, surface mobile layer is an active topic studied in molecular (*5*), metallic (*18*), and polymer glasses (*19*–*22*), especially for thin films. Whether it can be viewed as premelting has not been discussed. The thickness of the surface mobile layer for short-chain polymer glasses changes with temperature in a power law similar to Eq. 2 for crystal premelting but in a linear relation for long-chain polymer glasses (*72*). These suggest that the intensively studied surface mobile layer may be viewed as premelting for short-chain polymer glasses, but probably not for long-chain polymer glasses, because part of the long chains deep under the surface are entangled and frozen (*73*).

In contrast to crystal premelting, the glass surface exhibits an additional glassy layer defined by dynamic parameters, which is beyond the premelting theory. This layer exhibits the above surface liquid layer′s behavior of Eq. 2 (Figs. 3 and 6) but not Eqs. 3 and 7 (Figs. 4 and 6) as listed in Table 1. Furthermore, an interesting structural dynamic correlation analogous to mode-coupling equation is observed near the surface, but it varies with depth rather than with temperature in the mode-coupling relation (Fig. 5).

In addition, the CRR morphology evolution under fast heating is measured. The CRR morphology changes from compact to string-like particles, which is accompanied with the nonmonotonic surface glassy layer thickness change (Fig. 7H), similar to the CRR morphology changes observed in bulk accompanied with a nonmonotonic change of dynamic correlation length in (*25*, *26*). CRRs propagate toward the bulk, and thus they are elongated normal to the free surface in deeper regions. CRRs have slightly lower local densities, and therefore they bring free volumes into the bulk to facilitate the melting. This is similar to the opposite propagations of CRRs (from bulk toward surface) in a reverse process (vapor deposition growth of the glass) in (*27*).

Table 1. Comparison between crystals and the colloidal glasses in premelting and melting.

Similarities between crystals and glasses		Only observed in glasses
Premelting $\Longrightarrow$ stable liquid layer	Melting $\Longrightarrow$ propagating melting front	Additional glassy layer
Thickness $d_1 \propto (T/T_g - 1)^{\alpha_1}$ (Eq. 2 and Figs. 3 and 6)	Constant speed and width of melting front (Fig. 7)	Thickness $d_2 \propto (T/T_g - 1)^{\alpha_2}$ (Eq. 2 and Figs. 3 and 6)
Centrosymmetric profiles of structural parameters [e.g., $\tilde{\rho}(y)$ and $\tilde{s}_2(y)$; Eq. 3 and Figs. 4 and 6]	Centrosymmetric profiles of structural parameters [e.g., $\tilde{\rho}(y)$ and $\tilde{s}_2(y)$; Eq. 3 and Fig. 7]	Noncentrosymmetric profiles of dynamic parameters {e.g., $\log[DW(y)]$; Eqs. 4 and 5 as well as Figs. 4 and 6}
Structural parameters at vapor interface $\tilde{\rho}_{y=y'_s}, \tilde{s}_{2,y=y'_s} \propto (T/T_g - 1)^{\beta_{\rho,s_2}}$ (Eq. 7 and Figs. 3 and 6)	\	Dynamic parameters at vapor interface do not follow Eq. 7

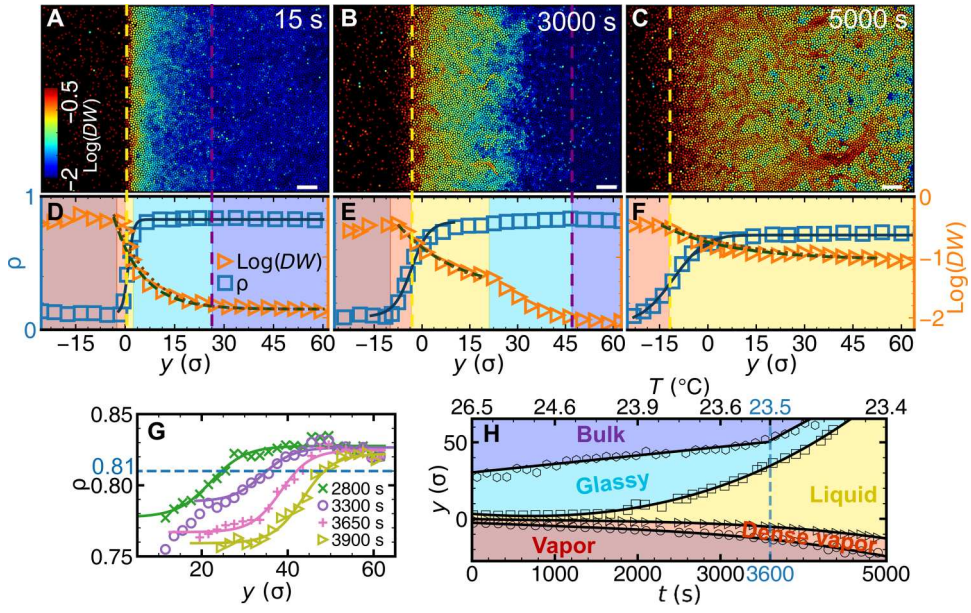

Fig. 7. Surface melting under the fast temperature change. (**A** to **C**) The monolayer sample colored by log(*DW*) at different times (also see movie S3). Scale bars, 20 μm. (**D** to **F**) ρ(*y*) and log[*DW*(*y*)] of (A) to (C) fitted by Eqs. 3 (solid curves) as well as 4 (dashed curves) and 5 (dotted curves), respectively (also see movie S4). They share the same double *y* axes. The colored regions are labeled in (H). (**G**) Density profiles across the glassy layer at different times fitted with Eq. 3 (solid curves). (**H**) Evolution of the surface layers.

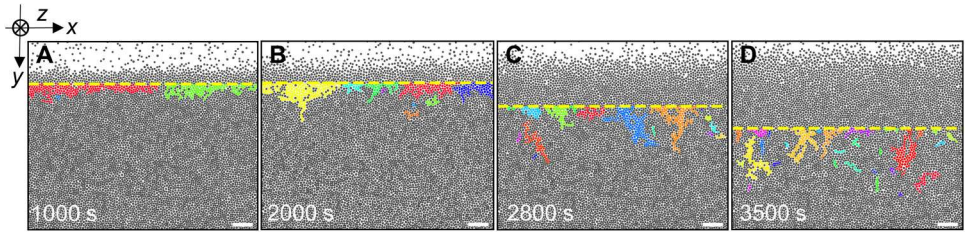

Fig. 8. CRRs on the surface for monolayer glass under fast temperature change. (**A** to **D**) Different cooperative rearrangement regions (CRRs) in the monolayer are labeled by different colors at 1000, 2000, 2800, and 3500 s. Scale bars, 20 μm.

Monolayer and multilayer glasses exhibit similar premelting and melting behaviors, indicating that the dimensionality effect is not prominent for glasses. This phenomenon is in accordance with the similar behaviors for 2D and 3D bulk glasses (*40*, *41*) and in contrast to the distinct premelting and melting behaviors for monolayer and bilayer crystals (*23*, *46*).

MATERIALS AND METHODS

Interaction between colloidal spheres

Nonfluorescent liquid dye (D98010 Chromatint jet black 1990, Chromatech Incorporated) is heated at 75°C for 7 hours and sonicated for 1 min. It is then added, 23% by volume, into the aqueous PMMA colloidal suspension (PAMMA-R, microParticles GmbH) with 30% volume fraction of PMMA spheres. The dye induces a depletion-like attraction among PMMA spheres, because its strength increases with the dye concentration and the measured attraction agrees with the Oosawa-Asakura model of depletion attraction (*23*). Without the dye, PMMA spheres exhibit no attraction.

We measure the radial distribution function $g(r) = \frac{1}{n^2}\langle \rho(\vec{r}' + \vec{r}, t)\rho(\vec{r}', t)\rangle$ of a dilute monolayer of monodispersed PMMA spheres at equilibrium (fig. S1A) to calculate their pair interaction (Fig. 1 and fig. S1B) (*74*). $\vec{r}$ is particle position, $\rho(\vec{r}, t) = \sum_{j=1}^{N(t)} \delta[\vec{r} - \vec{r}_j(t)]$, $n = N/A$ is the area density in a field of view containing N particles on average, and $\langle\,\rangle$ is the average over angles and time. Note that the small effects of the diffraction rings in the bright-field image analysis (*75*) and polydispersity have been corrected in the measurement of $g(r)$. According to the Ornstein-Zernike integral equation in the liquid structure theory (*74*, *75*), $U(r)$ is calculated from $g(r)$ by either the Percus-Yevick (PY) approximation or hypernetted-chain (HNC) approximation (*76*)

$$U(r) = -k_B T \ln[g(r)] + \begin{cases} k_B T n I(r) & \text{(HNC)} \\ k_B T \ln[1 + nI(r)] & \text{(PY)} \end{cases} \quad (8)$$

where $I(r) = \int_A [g(r') - 1 - nI(r)][g(|\vec{r}' - \vec{r}\,|) - 1]d^2r'$. PY and HNC are more accurate for hard and soft potentials, respectively. They are accurate only for low-density gas phase at equilibrium, and the iteration in the algorithm converges at area fractions below 15%. Thus, our area fractions are about 10% for the samples of the $U(r)$ measurements. $U(r)$ from the two approximations is highly consistent, suggesting that the calculation is reliable.

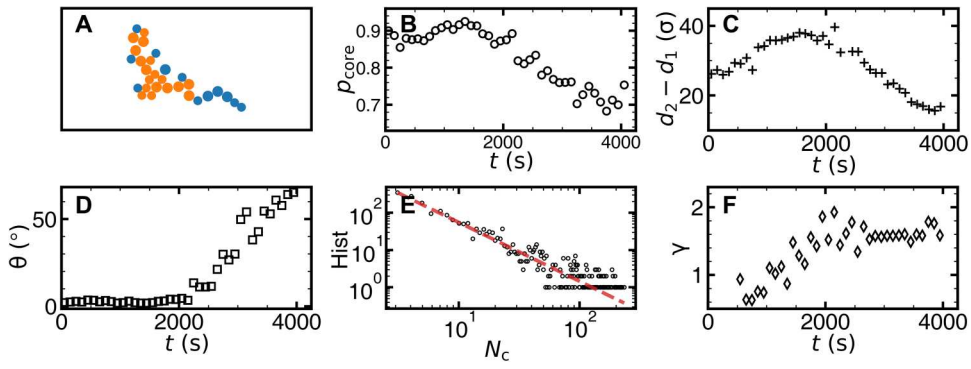

Fig. 9. CRR properties for the monolayer sample. (**A**) An example of CRR with core-like particles (orange) and string-like particles (blue). (**B**) Evolution of the fraction of core-like particles in CRRs. (**C**) Evolution of the glassy layer thickness $d_2 - d_1$. (**D**) The orientation θ of CRR's long axis relative to the glass surface. θ is weighted average by CRR size and aspect ratio. (**E**) The histogram (hist) of CRR size N_c during [3000 s, 3100 s] fitted by the power law (dashed red line) with the exponent γ = 1.58. (**F**) γ(t) from the size distributions of CRRs. Each data point is averaged over the time interval [t − 50 s, t + 50 s]. Note that the effective temperature increases with t, because the real temperature decreases with t.

This algorithm assumes that $U(r)$ is pairwise additive, which may not exactly hold in dense colloids. Nevertheless, the measured $U(r)$ describes that the attraction is tunable. The attraction strength U_{min}, i.e., the minimum of $U(r)$, is at r = 2.6 and 3.4 μm for small and large particles, respectively (fig. S1B). Thus, the attraction range is 0.5 μm for both particles, which is robust under different temperatures. Figure S1B shows that the effective temperature $T_{eff} = k_B T/|U_{min}(T)|$ linearly decreases with T.

Sample preparation

Binary PMMA spheres are used to avoid crystallization. The number ratio of large particles to small particles ranges from 40:60 to 60:40 in all the 10 samples of monolayer, bilayer, and trilayer glasses. Each kind of sphere has a small polydispersity of 2.2%. The sample preparation process is schematically shown in fig. S2. A colloid droplet is placed on a glass coverslip and covered by another coverslip (fig. S2A). We use coverslips instead of glass slides, because rigorously cleaned coverslips by deionized water and flame can effectively avoid particle sticking. The sample is sealed by epoxy to fix the sample thickness (fig. S2B). The sample thickness can be controlled by the volume of the colloid droplet, e.g., 1.5 μl for the monolayer sample. The colloidal droplet is spread in the center of 22 × 22 mm^2 area of the coverslip due to capillary force. Although the two glass plates are not perfectly parallel in the whole centimeter-sized sample area, they are sufficiently parallel in the millimeter-sized region such that a monolayer (or bilayer or trilayer) can form in a millimeter-sized area. Figure S3 shows a schematic of a trilayer sample. The x and y directions are along and perpendicular to the surface of the colloidal glass, respectively. The z direction is perpendicular to the coverslips. Surface layers in the main text are along the y direction, whereas monolayer, bilayer, and trilayer samples refer to the number of layers in the z direction (fig. S3).

To make the colloid droplet spread into a monolayer, the initial particle density needs to be low. Thus, colloidal particles are in a vapor phase in a freshly made sample. To form a glass, the sample is tilted in gravity under the room temperature, such that particles sediment to the edge with the desired wall separation and form a dense liquid or glass (fig. S2C). The sample is then placed horizontally and relaxed for 1 day to dense liquid and vapor under the room temperature T = 23°C where particles have negligible attractions (fig. S2D). By increasing the sample temperature, i.e., enhancing the attraction, to the desired initial temperature for measurements, the liquid region starts to vitrify into a glass and continues to grow through the slow layer-by-layer vapor deposition for more than 10 hours until the vapor phase is nearly depleted (fig. S2, E and F, and movie S1). The measurement is under quasi-equilibrium condition after a long-time equilibration without gravity. Sedimentation is commonly used for colloidal crystal fabrication and bulk studies, while the surface studies are limited and during the sedimentation processes for glasses (*27*) and crystals (*77*).

Temperature change

The objective heater (Bioptechs) with a 0.1°C resolution heats a sample area of a circle with a diameter of 10 mm. The temperature gradient at the edge of the heated region can pump the ambient dye into the heated region via thermophoresis, thereby enhancing the attraction. For the slow temperature change, T decreases at 0.2°C per step, and the sample is equilibrated for 1 to 3 hours at each step. For the fast temperature change, although the temperature controller is abruptly set across the glass transition temperature, the measured sample temperature decreases at a rate of about 10^{-3} to 10^{-2}°C/s because of the slow heat conduction of the objective, coverslips, and air (see fig. S4).

Relaxation time

The structural relaxation time τ is measured from the decay time of the self-intermediate scattering function $F_q(t)$ (fig. S9). At depth y, $F_q(y)$ is defined as (*78*)

$$F_q(y,t) = \langle e^{i\vec{q}\cdot[\vec{r}_i(t_0+t) - \vec{r}_i(t_0)]} \rangle_{t_0,i} \quad (9)$$

where $\vec{r}_i(t)$ is the position of particle i at time t, $\vec{q}$ is the first peak position of the structure factor of the bulk glass, and $\langle\ \rangle_{t_0,i}$ denotes the ensemble average over particles in the stripe at y and at the initial t_0. $F_q(t)$ reflects the particles' motions at lag time t on a length scale $2\pi/q$ and can be directly measured in the scattering experiment (*78*). $F_q(t)$ at different y can be fitted by $F_q(t) \sim e^{-(t/\tau)^\beta}$ with the relaxation time τ(y).

Local structural entropy

For a binary system (*79*), the two-point structural entropy $s_{2i} = -\frac{1}{2}\sum_{\nu}\rho_{\nu}\int d\vec{r}\{g_{\nu i}(\vec{r})\ln[g_{\nu i}(\vec{r})] - [g_{\nu i}(\vec{r}) - 1]\}$, where ρ_{ν} is the local number density of large or small particles, ν represents large or small particle, and $g_{\nu i}(\vec{r})$ is the radial distribution function of particle i. We choose the cutoff distance $r = 2.5\ \sigma$ for the integration, because $g(r > 2.5\ \sigma) \simeq 1$, and thus the long-ranged part barely affects s_2 (*36*).

Mean square displacement

Particle dynamics are often characterized by the mean square displacement (MSD)

$$\mathrm{MSD}(t) = \langle \Delta r^2(t) \rangle = \langle [\vec{r}_i(t' + t) - \vec{r}_i(t')]^2 \rangle \tag{10}$$

where $\langle\ \rangle$ is the average over time and particles in the chosen region. The measured MSD in fig. S10 shows that the out-of-cage time is about 30 s for particles near the surface ($y = 10\ \sigma$).

Cage-relative Debye-Waller factor

Besides the Debye-Waller factor, we also calculate the cage-relative Debye-Waller factor (*39*)

$$DW_{\mathrm{cri}}(t) = \sqrt{\langle [\vec{r}_i'(t) - \langle \vec{r}_i'(t) \rangle]^2 \rangle}/\sigma \tag{11}$$

where $\langle \vec{r}_i'(t) \rangle$ is the average position of particle i during $[t - t_0/2, t + t_0/2]$. It is different from the DW factor measured in the laboratory frame in which each particle's position is described in its local frame defined by the mean position of its N nearest neighbors: $\vec{r}_i' \equiv \vec{r}_i - \sum_j \vec{r}_j/N$. Thus, the effect of long-wavelength fluctuations is excluded in DW_{cr}.

Parameter normalization

$\mathrm{Log}(DW)$ is normalized into [0, 1] as

$$\log(\tilde{DW}) \equiv \frac{\log[DW(y)] - \log(DW)_{\mathrm{v}}}{\log(DW)_{\mathrm{b}} - \log(DW)_{\mathrm{v}}} \tag{12}$$

where subscripts "b" and "v" represent the values in bulk glass and vapor, respectively. $\log[\tilde{DW}(y)]$ increases with y, whereas $\log[DW(y)]$ decreases with y, because $\log(DW)_{\mathrm{b}} - \log\ (DW)_{\mathrm{v}} < 0$. Other parameters are similarly normalized.

Cooperative rearrangement regions

The fuzzy sphere model assumes that a CRR contains a compact core surrounded by a ramified string-like shell (*66*). The string-like shell and the compact core are predicted (*66*) and observed (*26*) to dominate at low and high temperatures, respectively. A particle is labeled core-like only if it has at least three nearest neighbors in the CRR and at least two of them have at least three nearest neighbors in the CRR; otherwise, it is labeled as string-like particles (Fig. 9) (*26*).

Supplementary Materials

This PDF file includes:

Supplementary Text
Sections S1 to S5
Figs. S1 to S23
Legends for movies S1 to S4
References

Other Supplementary Material for this manuscript includes the following:

Movies S1 to S4

REFERENCES AND NOTES

1. M. Lulli, C.-S. Lee, H.-Y. Deng, C.-T. Yip, C.-H. Lam, Spatial heterogeneities in structural temperature cause Kovacs' expansion gap paradox in aging of glasses. *Phys. Rev. Lett.* **124**, 095501 (2020).
2. G. Biroli, J. P. Garrahan, Perspective: The glass transition. *J. Chem. Phys.* **138**, 12A301 (2013).
3. X. Monnier, D. Cangialosi, B. Ruta, R. Busch, I. Gallino, Vitrification decoupling from α-relaxation in a metallic glass. *Sci. Adv.* **6**, eaay1454 (2020).
4. M. Wang, K. Zhang, Z. Li, Y. Liu, J. Schroers, M. D. Shattuck, C. S. O'Hern, Asymmetric crystallization during cooling and heating in model glass-forming systems. *Phys. Rev. E Stat. Nonlin. Soft Matter Phys.* **91**, 032309 (2015).
5. S. F. Swallen, K. Traynor, R. J. McMahon, M. D. Ediger, T. E. Mates, Stable glass transformation to supercooled liquid via surface-initiated growth front. *Phys. Rev. Lett.* **102**, 065503 (2009).
6. C. Eisenmann, C. Kim, J. Mattsson, D. A. Weitz, Shear melting of a colloidal glass. *Phys. Rev. Lett.* **104**, 035502 (2010).
7. R. L. Jack, L. Berthier, The melting of stable glasses is governed by nucleation-and-growth dynamics. *J. Chem. Phys.* **144**, 244506 (2016).
8. E. Flenner, L. Berthier, P. Charbonneau, C. J. Fullerton, Front-mediated melting of isotropic ultrastable glasses. *Phys. Rev. Lett.* **123**, 175501 (2019).
9. A. Vila-Costa, J. Ràfols-Ribé, M. González-Silveira, A. F. Lopeandia, L. Abad-Muñoz, J. Rodríguez-Viejo, Nucleation and growth of the supercooled liquid phase control glass transition in bulk ultrastable glasses. *Phys. Rev. Lett.* **124**, 076002 (2020).
10. C. Rodríguez-Tinoco, M. Gonzalez-Silveira, J. Ràfols-Ribé, A. Vila-Costa, J. C. Martinez-Garcia, J. Rodríguez-Viejo, Surface-bulk interplay in vapor-deposited glasses: Crossover length and the origin of front transformation. *Phys. Rev. Lett.* **123**, 155501 (2019).
11. K. L. Kearns, M. D. Ediger, H. Huth, C. Schick, One micrometer length scale controls kinetic stability of low-energy glasses. *J. Phys. Chem. Lett.* **1**, 388–392 (2010).
12. A. Wisitsorasak, P. G. Wolynes, Fluctuating mobility generation and transport in glasses. *Phys. Rev. E Stat. Nonlin. Soft Matter Phys.* **88**, 022308 (2013).
13. R. Gutiérrez, J. P. Garrahan, Front propagation versus bulk relaxation in the annealing dynamics of a kinetically constrained model of ultrastable glasses. *J. Stat. Mech.* **2016**, 074005 (2016).
14. S. Léonard, P. Harrowell, Macroscopic facilitation of glassy relaxation kinetics: Ultrastable glass films with frontlike thermal response. *J. Chem. Phys.* **133**, 244502 (2010).
15. J. G. Dash, A. W. Rempel, J. S. Wettlaufer, The physics of premelted ice and its geophysical consequences. *Rev. Mod. Phys.* **78**, 695–741 (2006).
16. M. D. Ediger, Perspective: Highly stable vapor-deposited glasses. *J. Chem. Phys.* **147**, 210901 (2017).
17. Q. Zheng, Y. Zhang, M. Montazerian, O. Gulbiten, J. C. Mauro, E. D. Zanotto, Y. Yue, Understanding glass through differential scanning calorimetry. *Chem. Rev.* **119**, 7848–7939 (2019).
18. J. Ma, C. Yang, X. Liu, B. Shang, Q. He, F. Li, T. Wang, D. Wei, X. Liang, X. Wu, Y. Wang, F. Gong, P. Guan, W. Wang, Y. Yang, Fast surface dynamics enabled cold joining of metallic glasses. *Sci. Adv.* **5**, eaax7256 (2019).
19. R. D. Priestley, C. J. Ellison, L. J. Broadbelt, J. M. Torkelson, Structural relaxation of polymer glasses at surfaces, interfaces, and in between. *Science* **309**, 456–459 (2005).
20. M. D. Ediger, J. A. Forrest, Dynamics near free surfaces and the glass transition in thin polymer films: A view to the future. *Macromolecules* **47**, 471–478 (2014).
21. Y. Chai, T. Salez, J. D. McGraw, M. Benzaquen, K. Dalnoki-Veress, E. Raphael, J. A. Forrest, A direct quantitative measure of surface mobility in a glassy polymer. *Science* **343**, 994–999 (2014).
22. F. Chen, C.-H. Lam, O. K. C. Tsui, The surface mobility of glasses. *Science* **343**, 975–976 (2014).
23. B. Li, F. Wang, D. Zhou, Y. Peng, R. Ni, Y. Han, Modes of surface premelting in colloidal crystals composed of attractive particles. *Nature* **531**, 485–488 (2016).
24. G. L. Hunter, E. R. Weeks, The physics of the colloidal glass transition. *Rep. Prog. Phys.* **75**, 066501 (2012).
25. W. Kob, S. Roldán-Vargas, L. Berthier, Non-monotonic temperature evolution of dynamic correlations in glass-forming liquids. *Nat. Phys.* **8**, 164–167 (2012).
26. K. Hima Nagamanasa, S. Gokhale, A. K. Sood, R. Ganapathy, Direct measurements of growing amorphous order and non-monotonic dynamic correlations in a colloidal glass-former. *Nat. Phys.* **11**, 403–408 (2015).

27. X. Cao, H. Zhang, Y. Han, Release of free-volume bubbles by cooperative-rearrangement regions during the deposition growth of a colloidal glass. *Nat. Commun.* **8**, 362 (2017).
28. J. R. Savage, D. W. Blair, A. J. Levine, R. A. Guyer, A. D. Dinsmore, Imaging the sublimation dynamics of colloidal crystallites. *Science* **314**, 795–798 (2006).
29. D. Bonn, J. Otwinowski, S. Sacanna, H. Guo, G. Wegdam, P. Schall, Direct observation of colloidal aggregation by critical Casimir forces. *Phys. Rev. Lett.* **103**, 156101 (2009).
30. P. J. Santos, P. A. Gabrys, L. Z. Zornberg, M. S. Lee, R. J. Macfarlane, Macroscopic materials assembled from nanoparticle superlattices. *Nature* **591**, 586–591 (2021).
31. A. Yethiraj, A. van Blaaderen, A colloidal model system with an interaction tunable from hard sphere to soft and dipolar. *Nature* **421**, 513–517 (2003).
32. S. F. Swallen, K. L. Kearns, M. K. Mapes, Y. S. Kim, R. J. McMahon, M. D. Ediger, T. Wu, L. Yu, S. Satija, Organic glasses with exceptional thermodynamic and kinetic stability. *Science* **315**, 353–356 (2007).
33. J. C. Crocker, D. G. Grier, Methods of digital video microscopy for colloidal studies. *J. Colloid Interface Sci.* **179**, 298–310 (1996).
34. A. Baranyai, D. J. Evans, Direct entropy calculation from computer simulation of liquids. *Phys. Rev. A* **40**, 3817–3822 (1989).
35. D. M. Sussman, S. S. Schoenholz, E. D. Cubuk, A. J. Liu, Disconnecting structure and dynamics in glassy thin films. *Proc. Natl. Acad. Sci. U.S.A.* **114**, 10601–10605 (2017).
36. H. Tanaka, T. Kawasaki, H. Shintani, K. Watanabe, Critical-like behaviour of glass-forming liquids. *Nat. Mater.* **9**, 324–331 (2010).
37. R. E. Nettleton, M. S. Green, Expression in terms of molecular distribution functions for the entropy density in an infinite system. *J. Chem. Phys.* **29**, 1365–1370 (1958).
38. I. Borzsák, A. Baranyai, On the convergence of Green's entropy expansion. *Chem. Rev.* **165**, 227–230 (1992).
39. S. Mazoyer, F. Ebert, G. Maret, P. Keim, Dynamics of particles and cages in an experimental 2D glass former. *Europhys. Lett.* **88**, 66004 (2009).
40. S. Vivek, C. P. Kelleher, P. M. Chaikin, E. R. Weeks, Long-wavelength fluctuations and the glass transition in two dimensions and three dimensions. *Proc. Natl. Acad. Sci. U.S.A.* **114**, 1850–1855 (2017).
41. H. Shiba, Y. Yamada, T. Kawasaki, K. Kim, Unveiling dimensionality dependence of glassy dynamics: 2D infinite fluctuation eclipses inherent structural relaxation. *Phys. Rev. Lett.* **117**, 245701 (2016).
42. S. S. Schoenholz, E. D. Cubuk, D. M. Sussman, E. Kaxiras, A. J. Liu, A structural approach to relaxation in glassy liquids. *Nat. Phys.* **12**, 469–471 (2016).
43. J. Mattsson, H. M. Wyss, A. Fernandez-Nieves, K. Miyazaki, Z. Hu, D. R. Reichman, D. A. Weitz, Soft colloids make strong glasses. *Nature* **462**, 83–86 (2009).
44. H. Yuan, J. Yan, P. Gao, S. K. Kumar, O. K. C. Tsui, Microscale mobile surface double layer in a glassy polymer. *Sci. Adv.* **8**, eabq5295 (2022).
45. R. Lipowsky, W. Speth, Semi-infinite systems with first-order bulk transitions. *Phys. Rev. B* **28**, 3983–3993 (1983).
46. X. Wang, B. Li, X. Xu, Y. Han, Surface roughening, premelting and melting of monolayer and bilayer crystals. *Soft Matter* **17**, 688–693 (2021).
47. G. Hantal, B. Fábián, M. Sega, P. Jedlovszky, Contribution of the two liquid phases to the interfacial tension at various water-organic liquid-liquid interfaces. *J. Mol. Liq.* **306**, 112872 (2020).
48. Y. Yang, M. Asta, B. B. Laird, Solid-liquid interfacial premelting. *Phys. Rev. Lett.* **110**, 096102 (2013).
49. N. P. Kryuchkov, N. A. Dmitryuk, W. Li, P. V. Ovcharov, Y. Han, A. V. Sapelkin, S. O. Yurchenko, Mean-field model of melting in superheated crystals based on a single experimentally measurable order parameter. *Sci. Rep.* **11**, 17963 (2021).
50. W. Schweika, H. Reichert, W. Babik, O. Klein, S. Engemann, Strain-induced incomplete wetting at CuAu(001) surfaces. *Phys. Rev. B* **70**, 041401 (2004).
51. J. E. Mueller, J. W. Gillespie Jr., S. G. Advani, Effects of interaction volume on x-ray line-scans across an ultrasonically consolidated aluminum/copper interface. *Scanning* **35**, 327–335 (2013).
52. Z. Fakhraai, J. A. Forrest, Measuring the surface dynamics of glassy polymers. *Science* **319**, 600–604 (2008).
53. K. S. Schweizer, D. S. Simmons, Progress towards a phenomenological picture and theoretical understanding of glassy dynamics and vitrification near interfaces and under nanoconfinement. *J. Chem. Phys.* **151**, 240901 (2019).
54. N. B. Tito, J. E. G. Lipson, S. T. Milner, Lattice model of mobility at interfaces: Free surfaces, substrates, and bilayers. *Soft Matter* **9**, 9403 (2013).
55. T. Salez, J. Salez, K. Dalnoki-Veress, E. Raphaël, J. A. Forrest, Cooperative strings and glassy interfaces. *Proc. Natl. Acad. Sci. U.S.A.* **112**, 8227–8231 (2015).
56. L. Berthier, G. Biroli, Theoretical perspective on the glass transition and amorphous materials. *Rev. Mod. Phys.* **83**, 587–645 (2011).
57. L. Santen, W. Krauth, Absence of thermodynamic phase transition in a model glass former. *Nature* **405**, 550–551 (2000).
58. F. Weysser, D. Hajnal, Tests of mode-coupling theory in two dimensions. *Phys. Rev. E Stat. Nonlin. Soft Matter Phys.* **83**, 041503 (2011).
59. Z. Zheng, R. Ni, F. Wang, M. Dijkstra, Y. Wang, Y. Han, Structural signatures of dynamic heterogeneities in monolayers of colloidal ellipsoids. *Nat. Commun.* **5**, 3829 (2014).
60. P. Gallo, M. Rovere, Relation between the two-body entropy and the relaxation time in supercooled water. *Phys. Rev. E Stat. Nonlin. Soft Matter Phys.* **91**, 012107 (2015).
61. C. Zhang, L. Hu, Y. Yue, J. C. Mauro, Fragile-to-strong transition in metallic glass-forming liquids. *J. Chem. Phys.* **133**, 014508 (2010).
62. F. Mallamace, C. Branca, C. Corsaro, N. Leone, J. Spooren, S.-H. Chen, H. E. Stanley, Transport properties of glass-forming liquids suggest that dynamic crossover temperature is as important as the glass transition temperature. *Proc. Natl. Acad. Sci. U.S.A.* **107**, 22457–22462 (2010).
63. H. Tanaka, H. Tong, R. Shi, J. Russo, Revealing key structural features hidden in liquids and glasses. *Nat. Rev. Phys.* **1**, 333–348 (2019).
64. S. Alvarado, M. Campagna, H. Hopster, Surface magnetism of Ni(100) near the critical region by spin-polarized electron scattering. *Phys. Rev. Lett.* **48**, 51–54 (1982).
65. H. Löwen, Melting, freezing and colloidal suspensions. *Phys. Rep.* **237**, 249–324 (1994).
66. J. D. Stevenson, J. Schmalian, P. G. Wolynes, The shapes of cooperatively rearranging regions in glass-forming liquids. *Nat. Phys.* **2**, 268–274 (2006).
67. Z. Zheng, R. Ni, Y. Wang, Y. Han, Translational and rotational critical-like behaviors in the glass transition of colloidal ellipsoid monolayers. *Sci. Adv.* **7**, eabd1958 (2021).
68. H. Peng, H. Liu, T. Voigtmann, Non-monotonic dynamic correlations beneath the surface of glass-forming liquids. *Phys. Rev. Lett.* **129**, 215501 (2021).
69. T. Lay, T. C. Wallace, Modern Global Seismology, in *International Geophysics Series* (Academic Press, San Diego, 1995), vol. 58.
70. D. R. Reid, I. Lyubimov, M. D. Ediger, J. J. de Pablo, Age and structure of a model vapour-deposited glass. *Nat. Commun.* **7**, 13062 (2016).
71. C. Rodríguez-Tinoco, M. González-Silveira, M. Barrio, P. Lloveras, J. L. Tamarit, J.-L. Garden, J. Rodríguez-Viejo, Ultrastable glasses portray similar behaviour to ordinary glasses at high pressure. *Sci. Rep.* **6**, 34296 (2016).
72. J. A. Forrest, K. Dalnoki-Veress, The glass transition in thin polymer films. *Adv. Colloid Interface Sci.* **94**, 167–195 (2001).
73. Z. Hao, A. Ghanekarade, N. Zhu, K. Randazzo, D. Kawaguchi, K. Tanaka, X. Wang, D. S. Simmons, R. D. Priestley, B. Zuo, Mobility gradients yield rubbery surfaces on top of polymer glasses. *Nature* **596**, 372–376 (2021).
74. S. H. Behrens, D. G. Grier, Pair interaction of charged colloidal spheres near a charged wall. *Phys. Rev. E Stat. Nonlin. Soft Matter Phys.* **64**, 050401 (2001).
75. M. Polin, D. G. Grier, Y. Han, Colloidal electrostatic interactions near a conducting surface. *Phys. Rev. E Stat. Nonlin. Soft Matter Phys.* **76**, 041406 (2007).
76. E. M. Chan, Two-dimensional Born-Green-Yvon and other integral equations. *J. Phys. C: Solid State Phys.* **10**, 3477–3486 (1977).
77. R. Ganapathy, M. R. Buckley, S. J. Gerbode, I. Cohen, Direct measurements of island growth and step-edge barriers in colloidal epitaxy. *Science* **327**, 445–448 (2010).
78. W. van Megen, T. C. Mortensen, S. R. Williams, J. Müller, Measurement of the self-intermediate scattering function of suspensions of hard spherical particles near the glass transition. *Phys. Rev. E Stat. Nonlin. Soft Matter Phys.* **58**, 6073–6085 (1998).
79. A. Samanta, S. M. Ali, S. K. Ghosh, New universal scaling laws of diffusion and Kolmogorov-Sinai entropy in simple liquids. *Phys. Rev. Lett.* **92**, 145901 (2004).
80. P. Luo, C. R. Cao, F. Zhu, Y. M. Lv, Y. H. Liu, P. Wen, H. Y. Bai, G. Vaughan, M. di Michiel, B. Ruta, W. H. Wang, Ultrastable metallic glasses formed on cold substrates. *Nat. Commun.* **9**, 1389 (2018).
81. H. Yoon, G. B. McKenna, Testing the paradigm of an ideal glass transition: Dynamics of an ultrastable polymeric glass. *Sci. Adv.* **4**, eaau5423 (2018).
82. L. Berthier, P. Charbonneau, E. Flenner, F. Zamponi, Origin of ultrastability in vapor-deposited glasses. *Phys. Rev. Lett.* **119**, 188002 (2017).
83. K. L. Ngai, M. Paluch, C. Rodríguez-Tinoco, Why is surface diffusion the same in ultrastable, ordinary, aged, and ultrathin molecular glasses? *Phys. Chem. Chem. Phys.* **19**, 29905–29912 (2017).
84. W. W. Mullins, Flattening of a nearly plane solid surface due to capillarity. *J. Appl. Phys.* **30**, 77–83 (1959).
85. Y. Li, W. Zhang, C. Bishop, C. Huang, M. D. Ediger, L. Yu, Surface diffusion in glasses of rod-like molecules posaconazole and itraconazole: Effect of interfacial molecular alignment and bulk penetration. *Soft Matter* **16**, 5062–5070 (2020).
86. Y. Zhang, Z. Fakhraai, Invariant fast diffusion on the surfaces of ultrastable and aged molecular glasses. *Phys. Rev. Lett.* **118**, 066101 (2017).

87. K. L. Kearns, P. Krzyskowski, Z. Devereaux, Using deposition rate to increase the thermal and kinetic stability of vapor-deposited hole transport layer glasses via a simple sublimation apparatus. *J. Chem. Phys.* **146**, 203328 (2017).
88. R. Blumenfeld, Disorder criterion and explicit solution for the disc random packing problem. *Phys. Rev. Lett.* **127**, 118002 (2021).
89. C. L. Klix, G. Maret, P. Keim, Discontinuous shear modulus determines the glass transition temperature. *Phys. Rev. X* **5**, 041033 (2015).
90. C. L. Klix, F. Ebert, F. Weysser, M. Fuchs, G. Maret, P. Keim, Glass elasticity from particle trajectories. *Phys. Rev. Lett.* **109**, 178301 (2012).
91. C. Rycroft, "Voro++: A three-dimensional voronoi cell library in C++" [Technical Report, Lawrence Berkeley National Lab. (LBNL), 2009].
92. L. Berthier, M. D. Ediger, How to "measure" a structural relaxation time that is too long to be measured? *J. Chem. Phys.* **153**, 044501 (2020).
93. H. Shintani, H. Tanaka, Universal link between the boson peak and transverse phonons in glass. *Nat. Mater.* **7**, 870–877 (2008).
94. S. Toxvaerd, J. Stecki, Density profiles at a planar liquid-liquid interface. *J. Chem. Phys.* **102**, 7163–7168 (1995).
95. S. Toxværd, *Statistical Mechanics*, K. Singer, Ed. (Royal Society of Chemistry, Cambridge, 1975), vol. 2, pp. 256–299.
96. H. Ramalingam, M. Asta, A. van de Walle, J. J. Hoyt, Atomic-scale simulation study of equilibrium solute adsorption at alloy solid-liquid interfaces. *Interface Sci.* **10**, 149–158 (2002).
97. D. Danilov, B. Nestler, M. Guerdane, H. Teichler, Bridging the gap between molecular dynamics simulations and phase-field modelling: Dynamics of a $[Ni_xZr_{1-x}]_{liquid}$–$Zr_{crystal}$ solidification front. *J. Phys. D: Appl. Phys.* **42**, 015310 (2009).
98. E. S. Wu, W. W. Webb, Critical liquid-vapor interface in SF_6. I. Thickness of the diffuse transition layer. *Phys. Rev. A* **8**, 2065–2076 (1973).
99. S. Fisk, B. Widom, Structure and free energy of the interface between fluid phases in equilibrium near the critical point. *J. Chem. Phys.* **50**, 3219–3227 (1969).
100. J. G. Dash, Surface melting. *Contemp. Phys.* **30**, 89–100 (1989).
101. A. Sepúlveda, S. F. Swallen, L. A. Kopff, R. J. McMahon, M. D. Ediger, Stable glasses of indomethacin and α,α,β-tris-naphthylbenzene transform into ordinary supercooled liquids. *J. Chem. Phys.* **137**, 204508 (2012).
102. C. Rodríguez-Tinoco, M. Gonzalez-Silveira, J. Ràfols-Ribé, A. F. Lopeandía, M. T. Clavaguera-Mora, J. Rodríguez-Viejo, Evaluation of growth front velocity in ultrastable glasses of Indomethacin over a wide temperature interval. *J. Phys. Chem. B* **118**, 10795–10801 (2014).
103. C. Rodríguez-Tinoco, J. Ràfols-Ribé, M. González-Silveira, J. Rodríguez-Viejo, Relaxation dynamics of glasses along a wide stability and temperature range. *Sci. Rep.* **6**, 35607 (2016).
104. C. T. Moynihan, A. J. Easteal, J. Wilder, J. Tucker, Dependence of the glass transition temperature on heating and cooling rate. *J. Phys. Chem.* **78**, 2673–2677 (1974).

Acknowledgments: We thank S.-T. Chui, O. Tsui, C.-H. Lam, F. Wang, H. Zhang, and H. Tang for their helpful discussions. **Funding:** This work was supported by Hong Kong RGC grants CRF-C6016-20G and GRF-16305822 and the Guangdong Basic and Applied Basic Research Foundation (grant no. 2020B1515120067). **Author contributions:** Y.H. and Q.Z. conceived and designed the research. Q.Z. performed the experiment and data analysis with the help from W.L., K.Q., and Y.H. Q.Z. and Y.H. wrote the paper. Y.H. supervised the work. All authors discussed the results. **Competing interests:** The authors declare that they have no competing interests. **Data and materials availability:** All data needed to evaluate the conclusions in the paper are present in the paper and/or the Supplementary Materials.

Submitted 29 September 2022
Accepted 13 February 2023
Published 17 March 2023
10.1126/sciadv.adf1101